Non-cascaded Robust Model Predictive Direct Speed Control Based on the Reconstruction Model and Third-Order ESO for SPMSM

Zhenrui Zhang, Xingyu Wang, Jing Xu, and Qingya Zhang

***Abstract*—This article presents a more robust model predictive direct speed control based on the third-order extended state observer (RMPDSC-TESO) method for surface-mounted permanent magnet synchronous motor (SPMSM) servo systems to attain a superior disturbance rejection performance and simplify parameter adjustment. First, by taking advantage of the fast current response to reconstruct the load disturbance, the disturbances in the motion and voltage equations are transformed into a unified equivalent current disturbance, thereby constructing a second-order speed ultralocal model. Subsequently, a TESO that only requires consideration of a single control parameter is adopted to estimate the speed control model's lumped disturbance, improving the system's robustness. Moreover, the deadbeat method is adopted to obtain the optimal voltage control solution. Then, by conducting derivations on the root locus and disturbance sensitive characteristics, the system's stability, anti-interference performance, and the influence of the input gain on the system's dynamic performance are demonstrated. Finally, experimental verification was carried out on a SPMSM test platform based on a DSP F28379D chip, and the results confirm the effectiveness of this control strategy in terms of dynamic performance and unmodeled disturbance suppression.**

***Index Terms*—Direct speed prediction control, permanent magnet synchronous motor (PMSM), third-order ESO, unmodeled disturbance suppression.**

I. Introduction

With high efficiency and excellent speed-control performance, permanent magnet synchronous motors (PMSMs) are widely used in various servo applications, especially in water-jet propulsion systems [1]. Model predictive control (MPC) uses a predictive function to constrain state variables and select the optimal output vector. Therefore, its performance is not restricted by the control bandwidth of the frequency-domain system [2]. MPC has advantages such as faster dynamic response and easier handling of nonlinear variable constraints, making it popular in PMSM control scenarios. Application of MPC includes model predictive torque control, model predictive current control [3], and model predictive direct speed control [4]. Regarding solution methods, they are divided into continuous set solutions [5] and finite control set solutions [6]. Considering computational performance, the continuous set usually adopts a deadbeat solution method to obtain the optimal control voltage [7]. Finite control set MPC retains the multiobjective optimization characteristics of MPC [8], but computational complexity requires more computing time. Meanwhile, its steady-state performance is worse than the deadbeat MPC. Therefore, the deadbeat solution method is now more widely used. In addition, both model predictive current control and model predictive torque control retain the speed PI controller. So, the control structure still exhibits a cascaded characteristic, and the dynamic characteristics of these two methods are basically the same [9]. However, the cascaded structure limits the system's dynamic and anti-interference performance, especially when the bandwidth of the speed loop cannot be increased [10].

With the advancement of control technology, the difference in control periods between the speed and current loops has gradually diminished and even vanished [11]. Therefore, current and speed can be incorporated into the same evaluation system to discard cascade control and achieve direct speed predictive control. For example, Preindl and Bolognani [12] proposed a model predictive direct speed control method based on a finite control set, breaking through the limitations of cascade linear controllers and achieving high-speed control dynamic characteristics. Fuentes et al. [4] used an extended Kalman filter to estimate system states and load disturbances, then proposed a centralized predictive control strategy that simultaneously controls all system variables, including mechanical and electrical variables, thus realizing direct speed control. Liu et al. [13] proposed a model predictive direct speed control strategy without a PI control unit. This strategy has excellent speed tracking ability and effectively reduces speed deviation. Zhang and He [14] designed a cost function with motor torque constraints and a voltage optimization scheme based on speed constraints, simplifying the selection process of weight coefficients. Although MPC has significant advantages over vector control methods in dynamic performance and parameter tuning

Received 18 August 2025; revised 31 October 2025; accepted 29 November 2025. Date of publication 3 December 2025; date of current version 25 February 2026. This work was supported in part by the National Natural Science Foundation of China under Grant 51979021, in part by Jiangsu University Collaborative Innovation Project under Grant XTCX202409 and Grant XTCX202407, in part by Jiangsu University of Science and Technology Doctoral Research Start-up Funds under Grant 1172932302, and in part by Basic science (Natural Science) Research Project of Higher Education in Jiangsu Province under Grant 24KJD470004. Recommended for publication by Associate Editor B. Singh. *(Corresponding author: Jing Xu.)*

The authors are with the Department of Marine Equipment and Technology Institute, Jiangsu University of Science and Technology, Zhenjiang 212003, China (e-mail: tabz00@just.edu.cn; 202200000207@just.edu.cn; xujing@just.edu.cn; 202200000212@just.edu.cn).

Color versions of one or more figures in this article are available at https://doi.org/10.1109/TPEL.2025.3639648.

Digital Object Identifier 10.1109/TPEL.2025.3639648

process, the system's parameter time-varying and unmodeled disturbances remain key factors restricting its performance. Currently, suppression methods are mainly designed based on the control structure characteristics of current control and speed control.

The steady-state performance is vulnerable to the impacts of modeling accuracy and load disturbances. For example, the saturation inductance caused by an increase in current can lead to current harmonics [15], [16]. In current control, parameter identification and prediction error compensation are crucial to address parameter time-varying disturbances. However, online parameter identification algorithms generally require high computational loads and cannot be adapted to all control systems. Therefore, Zhou et al. [17] decoupled the stator inductance and flux linkage based on the current prediction error model to reduce the impact of parameter mismatch. Yuan et al. [18] proposed a current change update mechanism, which can update the modified prediction equation within each sampling period, thus suppressing parameter time-varying disturbances. Nevertheless, prediction error compensation depends on the sampling accuracy of the system, and it is difficult to meet the requirements of systems with unmodeled disturbances.

Many scholars have proposed methods for suppressing parameter time-varying disturbances based on disturbance observers. Establishing a disturbance observer using a reconstructed ultralocal model of the motor system has advantages in suppressing the lumped disturbances of the system [19]. Liu and Li [20] optimized the servo control structure of the PMSM using an ESO, suppressing the impact of disturbances on the motor performance, but did not eliminate the cascade structure. The model-free predictive current control methods proposed based on ESO in [21], [22], and [23], effectively reduced the impact of prediction errors and improved the system's robustness. On this basis, to solve the problem of controller gain, Wu et al [24] analyzed the influence of the input gain of the ESO on control performance and proposed an adaptive gain control method. These methods significantly enhance the robustness of model predictive current control and suppress parameter time-varying and unmodeled disturbances.

To further solve the problem of parameter time-varying disturbances and load disturbances in model predictive direct speed control, Chen et al. [25], Gao et al. [26], and Zhang et al. [27] proposed a predictive speed control method based on the cascaded disturbance compensation structure (PSC-CDCS) by identifying the lumped disturbances of the speed loop and current loop to suppress the parameter time-varying and unmodeled disturbances in speed and current control. However, this method must consider the coupling problem during the parameter tuning of the current and speed observers. Besides, it is not a truly cascade-free control method, and its dynamic performance still has room for improvement. Given this, this article conducts research on control structure and performance optimization.

This article proposes a robust direct speed control method based on a TESO to reduce the impacts of parameter variations and load disturbances on speed predictive control. The main contributions of this method are as follows:

1) By reconstructing the control equations of motor current and speed, the speed disturbance is equivalently converted into a current disturbance, thus simplifying the control structure. Meanwhile, a TESO matching the reconstructed model is designed, which avoids problems such as the cascade structure of inner and outer loops and improper parameter matching, and enhances the dynamic response of the speed.
2) The influences of all parameters are grouped into one control gain to reduce disturbance variables and mitigate the adverse effects on the system when the inductance and flux-linkage parameters change simultaneously under high-load conditions.
3) The disturbance sensitivity transfer function is established to analyze the stability and interference ability of the system. The influence of the change of observation gain on the system's dynamic and steady-state performance is explained with the root locus. The deadbeat method is used to solve the reconstructed prediction model directly, and the computational efficiency of the processor is improved by combining it with the reconstructed structure.

The rest of this article is organized as follows. Section II introduces the design process of the speed reconstruction mathematical model of the SPMSM. In Section III, based on the reconstructed speed model considering parameter variations and unmodeled disturbances, the corresponding TESO is proposed, and the stability of the observer and its influence on the system are analyzed. Section IV uses an experimental platform to verify the advantages of the proposed control method in terms of steady-state, dynamic, and robustness. Finally, Section V concludes this article.

II. Design of Reconstructed Ultra-Local Speed Prediction Model

The ideal mathematical model of the SPMSM does not consider unmodeled and parameter variation disturbances during the design, which may lead to prediction errors in the MPC algorithm. Therefore, this section introduces unknown disturbances into the prediction model and reconstructs the motor's second-order speed-prediction ultra-local model using the disturbance-equivalence principle.

In the rotating coordinate system, the mathematical model of PMSM is [28]

$$\begin{aligned}\frac{d\omega_r}{dt} &= \frac{T_e}{J} \underbrace{-\frac{(T_l + B\omega_r)}{J}}_{f_\omega} \\ \frac{di_q}{dt} &= \frac{1}{L_q}v_q \underbrace{-\frac{R_s}{L_q}i_q - \frac{\omega_e}{L_q}(i_d L_d + \psi)}_{f_q} \\ \frac{di_d}{dt} &= \frac{1}{L_d}v_d \underbrace{-\frac{R_s}{L_d}i_d + \frac{L_q}{L_d}\omega_e i_q}_{f_d}\end{aligned} \tag{1}$$

where v_d and v_q are the d-axis and q-axis voltages, i_d and i_q are the d-axis and q-axis currents, L_d and L_q are the d-axis

and q-axis inductances (for SPMSM: $L_s = L_d = L_q$), R_s is the stator resistance, ψ is the permanent magnet flux, and ω_e is the electrical angular velocity. ω_r, T_e, T_l, B, and J represent the motor's mechanical angular velocity, torque, load torque, viscous damping coefficient, and moment of inertia, respectively. To construct an ultralocal model [22], f_ω, f_d, and f_q are defined as the disturbances of the system.

The motion equation of the motor is

$$T_e = 1.5P\psi i_q \tag{2}$$

where P represents the motor's number of pole pairs.

By using the ultralocal modeling concept, the ideal models presented in (1) and (2) can be equivalently described as the relationship between input and disturbance variables. Therefore, the equivalent model of the system can be described as follows:

$$\begin{cases} \dot{\omega}_r = \alpha_\omega i_q + f_\omega \\ \dot{i}_d = \alpha_d v_d + f_d \\ \dot{i}_q = \alpha_q v_q + f_q \end{cases} \tag{3}$$

where α_ω, α_d, and α_q are the gain coefficients of the input variables, and $\alpha_\omega = 1.5P\psi/J$, $\alpha_d = 1/L_d$, $\alpha_q = 1/L_q$.

Based on the simplification method of traditional control theory, the speed disturbance in (3) is equivalent to the current disturbance to improve the controller's effect in suppressing speed disturbances. In addition, the decoupling of d-axis and q-axis currents is achieved by establishing an observer to ignore the indirect influence of d-axis current on speed. Therefore, a new current variable is defined by

$$i_{\text{new}} = \dot{\omega}_r = \alpha_\omega i_\omega + f_\omega \tag{4}$$

where i_{new} is the reconstructed current of speed prediction.

Furthermore, the q-axis current can be represented by it

$$i_q = \frac{i_{\text{new}}}{\alpha_\omega} - \frac{f_\omega}{\alpha_\omega}. \tag{5}$$

By rearranging (3) and (5), the restructured second-order control model for motor speed can be obtained as

$$\begin{cases} \dot{\omega}_r = i_{\text{new}} \\ \dot{i}_{\text{new}} = \alpha_\omega \alpha_q v_q + \underbrace{\alpha_\omega f_q + \dot{f}_\omega}_{f_i} \end{cases} \tag{6}$$

where f_i is the lumped disturbances in the second-order restructured speed model.

By rearranging (6), the restructured speed control model can be obtained as

$$\begin{cases} \dot{\omega}_r = i_{\text{new}} \\ \dot{i}_{\text{new}} = \alpha_i v_q + f_{\text{i}} \end{cases} \tag{7}$$

where $\alpha_i = \alpha_\omega \alpha_q$.

The speed and current are within the same control cycle in systems. By utilizing forward Euler discretization, (7) can be obtained as

$$\begin{cases} \omega_r(p) = T'_s i_{\text{new}}(k+1) + \omega_r(k) \\ i_{\text{new}}(k+1) = T_{\text{s}}(\alpha_i v_q + f_i(k)) + i_{\text{new}}(k) \end{cases} \tag{8}$$

where T_s and T_s' represent the discrete time of current and speed. $\omega_r(p)$ is the predicted speed based on the current and speed at the k moment. Although the speed and current update time are the same in the actual control system, the mechanical speed's response time is longer than the current's. Therefore, this article sets $T_s' = 10T_s$ to design the speed controller.

The predicted speed equation for the motor can be derived as follows:

$$\omega_r(p) = T'_s(T_s(\alpha_i v_q + f_i(k)) + i_{\text{new}}(k)) + \omega_r(k). \tag{9}$$

However, the values of $\omega_r(k+1)$, $f_i(k)$, and $i_{\text{new}}(k)$ cannot be directly obtained in the actual systems. The following section explores the methods for obtaining these variables by designing a TESO.

III. Direct Speed Prediction Control Based on TESO

This part introduces a TESO to obtain the disturbance term in (9) and proposes a low-pass filtering-based parameter configuration method. Subsequently, the stability and disturbance-rejection performance of the observer for system control are discussed.

A. Design of the TESO

The ESO can be designed with a corresponding observer model based on the order of the control model. A TESO can be designed for a second-order speed model [29].

$$\begin{cases} e = \hat{\omega}_r - \omega_r \\ \dot{\hat{\omega}}_r = \hat{i}_{\text{new}} - \beta_1 e \\ \dot{\hat{i}}_{\text{new}} = \hat{f}_i + \alpha_i v_q - \beta_2 e \\ \dot{\hat{f}}_i = -\beta_3 e \end{cases} \tag{10}$$

where $\hat{}$ represents the observer value of the variables. β_1, β_2, and β_3 are parameters of the ESO.

Assuming zero initial conditions and utilizing the Laplace transform, (13) can be derived as

$$\hat{f}_i = \beta_3 \frac{\omega_r s^2 - \alpha_i v_q}{s^3 + \beta_1 s^2 + \beta_2 s + \beta_3} \tag{11}$$

where $\omega_r s^2 - \alpha_i v_q$ is the actual lumped disturbance f_{i} of the motor. Therefore, (11) can be rewritten as

$$\frac{\hat{f}_i}{f_i} = \beta_3 \frac{1}{s^3 + \beta_1 s^2 + \beta_2 s + \beta_3}. \tag{12}$$

From (12), the frequency characteristics of the transfer function determine the observer's ability to observe the lumped disturbance. Since the lumped disturbance is typically low-frequency, it is reasonable to define (12) as a third-order low-pass filter. Therefore, the transfer function of the cascaded three first-order low-pass filters can be expressed as

$$\left(\frac{\omega}{\omega + s}\right)^3 = \frac{\omega^3}{s^3 + 3\omega s^2 + 3\omega^2 s + \omega^3}. \tag{13}$$

By analogy, the parameter configuration method for the observer can be defined as

$$\beta_1 = 3\omega, \beta_2 = 3\omega^2, \beta_3 = \omega^3. \tag{14}$$

As the transfer function of a single low-pass filter is stable, the cascaded combination of three low-pass filters with the same

transfer function also maintains stability. Hence, the stability of the TESO configured by (14) can be ensured.

When the assumed bandwidth of the observer configuration is set to ω_0, the gain formula for (13) is derived as follows:

$$\left|\left(\frac{\omega_0}{\omega_0+s}\right)^3\right| = \frac{{\omega_0}^3}{\sqrt{\left(3\,\omega{\omega_0}^2-\omega^3\right)^2+\left(3\,\omega^2\omega_0-{\omega_0}^3\right)^2}}. \tag{15}$$

In (15), the gain value is set to 0.707. At this point, the bandwidth corresponding to this gain is the actual bandwidth of the observer. Upon solving, the relationship between the real bandwidth ω and the set bandwidth ω_0 is

$$\omega = 0.51\omega_0. \tag{16}$$

Equation (16) reveals that the actual bandwidth is approximately half of the configured bandwidth. Therefore, to achieve more accurate disturbance observation, especially when the system disturbance frequency is known, it is recommended that when configuring the parameters of the ESO, the ω in (14) be set to twice the actual bandwidth.

Similarly, observation can be achieved by establishing a second-order ESO for a first-order d-axis current model [29]

$$\begin{cases} e_d = \hat{i}_d - i_d \\ \dot{\hat{i}}_d = \hat{f}_d + \alpha_d v_d - \beta_4 e_d \\ \dot{\hat{f}}_d = -\beta_5 e_d \end{cases}. \tag{17}$$

The transfer function of the observed disturbance and the actual disturbance is

$$\frac{\hat{f}_d}{f_d} = \frac{\beta_5}{s^2+s\beta_4+\beta_5}. \tag{18}$$

The configuration of parameters for the d-axis current control can be achieved by analogy to the parameters of a second-order low-pass filter. The following setup can be applied to defining a disturbance bandwidth ω_d for the d-axis current

$$\begin{aligned} \beta_4 &= 2\omega_d. \\ \beta_5 &= \omega_d^2 \end{aligned} \tag{19}$$

B. Stability and Disturbance Sensitivity Analysis of Speed Control

System performance can be analyzed by establishing the output of the controller and the actual motor mathematical model. First, the transfer function between the q-axis current and voltage of the motor, derived from (1), is as follows:

$$i_q(s) = \frac{v_q(s)}{L_s s + R_s}. \tag{20}$$

The transfer function of the speed loop is

$$\frac{\omega_r(s)}{i_q(s)} = \frac{3P\psi}{2} \times \frac{1}{Js}. \tag{21}$$

Under the assumption that the system has no delay, the prediction equation shown in (9) can be used to derive the q-axis voltage control solution. By utilizing the observation from the ESO and applying the deadbeat technique [30], the q-axis voltage controller is achieved by

$$v_q = \frac{1}{10\alpha_i T_s^2}\left(\omega_r^{\text{ref}} - \omega_r\right) - \frac{1}{\alpha_i T_s}\hat{i}_{\text{new}} - \frac{1}{\alpha_i}\hat{f}_i \tag{22}$$

After deriving the state equation of the ESO (10), the relationship between the observed value $\hat{i}_{\text{new}}$ and the system variables can be established by

$$\hat{i}_{\text{new}} = \frac{3\omega_r\omega^2 s^2 + a_i v_q s^2 + \omega_r\omega^3 s + 3\,a_i v_q \omega s}{s^3 + 3\omega s^2 + 3\omega^2 s + \omega^3}. \tag{23}$$

Combining the disturbance (11), the Laplace-transformed motor mathematical model (20) and (21), q-axis output voltage (22) and reconstruction current (23), the sensitivity transfer function from disturbance to speed can be derived as

$$\begin{aligned} \frac{f_q(s)}{\omega_r(s)} &= \frac{n_3 s^3 + n_2 s^2 + n_1 s}{d_5 s^5 + d_4 s^4 + d_3 s^3 + d_2 s^2 + d_1 s + d_0} \\ n_1 &= 45\psi P {T_s}^2\omega^2 + 45\psi P T_s\omega,\ n_2 = 45\psi P\omega {T_s}^2 + 15\psi P T_s \\ n_3 &= 15\psi P\,{T_s}^2,\ d_0 = JL_s\omega^3,\ d_1 = 10JL_sT_s\omega^3 + 3JL_s\omega^2 \\ d_2 &= 10JL_s{T_s}^2\omega^3 + 30JR_s{T_s}^2\omega^2 + 30JL_sT_s\omega^2 \\ &\quad + 30JR_sT_s\omega + 3JL_s\omega \\ d_3 &= 30JL_s{T_s}^2\omega^2 + 30JR_s{T_s}^2\omega + 30JL_sT_s\omega \\ &\quad + 10JR_sT_s + 2JL_s \\ d_4 &= 10JL_sT_s + 10JR_s{T_s}^2 + 30JL_s{T_s}^2\omega,\ d_5 = 10JL_s{T_s}^2. \end{aligned} \tag{24}$$

The Bode diagram of the transfer function obtained from (24), as depicted in Fig. 1, demonstrates that the bandwidth of the observer exerts a remarkable influence on the system's anti-interference ability. The greater the bandwidth, the stronger the system's capacity to suppress low-frequency harmonics, and the lower the sensitivity of disturbances to speed.

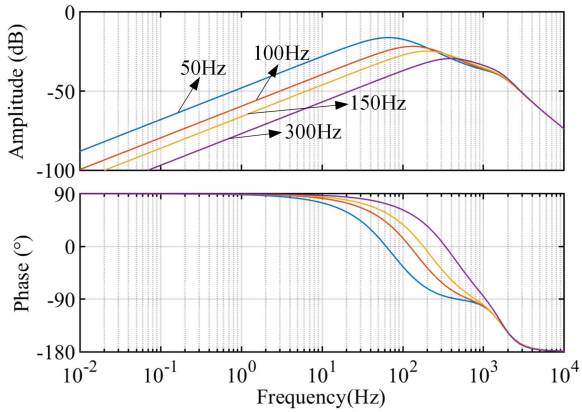

Fig. 1. System's disturbance rejection performance is based on different bandwidths in the TESO.

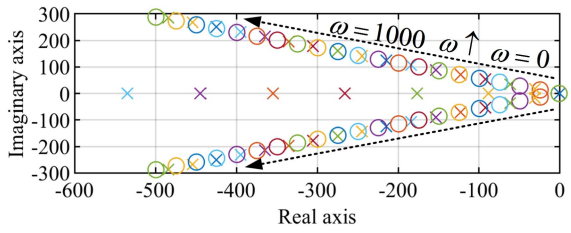

Fig. 2. The root locus diagram of the system when the bandwidth changes.

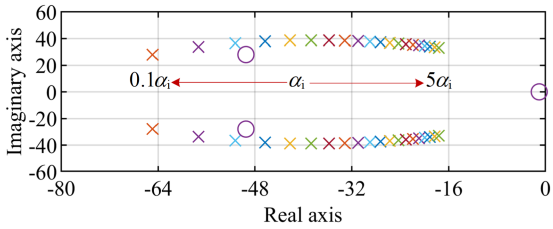

Fig. 3. Root locus diagram of the system when the input gain α_{i} changes.

The closed-loop transfer function of the further developed control system is as follows:

$$\begin{aligned}
&\frac{\omega_r(s)}{\omega_r^{\mathrm{ref}}(s)} = \frac{n_3+n_2+n_1+n_0}{d_5+d_4+d_3+d_2+d_1+d_0}\\
&n_0 = 3\psi P\omega^3, n_1 = 3\psi P\omega^3, n_2 = 9\psi P\omega^2, n_3 = 9\psi P\omega\\
&d_0 = 3\psi P\omega^3, d_1 = 30\,\psi PT_s\omega^3 + 9\psi P\omega^2\\
&d_2 = 30\psi PT_s{}^2\omega^3 + 60JR_sa_iT_s{}^2\omega^2 + 90\psi PT_s\omega^2\\
&\quad + 60JR_sa_iT_s\omega + 9\,\psi P\omega, d_3 = 60JL_sa_iT_s{}^2\omega^2\\
&\quad + 6J0R_sa_iT_s{}^2\omega\\
&\quad + 60JL_sa_iT_s\omega + 2J0R_sa_iT_s + 3\psi P,\\
&d_4 = 20JR_sT_s{}^2a_i + 20JL_sT_sa_i + 60JL_sT_s{}^2a_i\omega\\
&d_5 = 20JL_sT_s{}^2a_i. \qquad (25)
\end{aligned}$$

Analyze the root locus diagram of the characteristic roots of (25) changing with the bandwidth, as shown in Fig. 2. As the bandwidth increases, the root locus of the system moves to the left, and the stability is enhanced. This root locus indicates that a larger observer bandwidth can suppress a greater range of motor disturbances, thus improving the system's stability. However, in practical applications, an excessively high bandwidth can introduce high-frequency measurement noise through the feed-forward path, which is unfavorable to the stable control of the system.

Previous research [31] explored the update methods of controller and observer gains using the adaptive extremum-seeking method, providing an essential technology for systems with unknown parameters. Regarding the design of the optimality of the system with respect to α_i, further analysis can be carried out based on the root locus to achieve optimal dynamic control performance. As shown in Fig. 3, as α_i increases, the characteristic roots of the system shift to the right, shortening the distance from the imaginary axis and gradually reducing the system's stability margin. When the characteristic roots shift to the right, the absolute value of their real part decreases, causing the exponential decay term to decay more slowly and the settling time to become longer. Thus, it can be seen that the smaller the α_i, the more beneficial it is to the stability and dynamic performance of the system. However, as α_i decreases, the imaginary part of the characteristic roots decreases, and the oscillation frequency increases. Considering that the speed is relatively sensitive to low-frequency oscillations, an α_i that is too small is also not conducive to system control. Therefore, the controller and observer gains can be slightly less than the actual values (e.g., $0.8\alpha_i$) to achieve better dynamic performance.

C. Implementation of Robust Model Predictive Direct Speed Control

Robust model predictive direct speed control mainly focuses on the control of speed. Since the q-axis current has been reconstructed in the speed control, only the prediction and constraints of the speed and the d-axis current need to be considered. Its cost function is the sum of squares of the differences between the reference and predicted values. However, the deadbeat solution method is used in the solution process, substituting the reference values directly into the predicted values to calculate the control voltage directly. Although the update mechanisms of speed and current are the same in practical systems, the response time of speed is much shorter than that of current. Therefore, to compensate for the current delay, the estimated value at the (k+1)th moment is used to predict the speed of the next cycle

$$\omega_r(p) = T'_s(T_s(\alpha_i v_q + \hat{f}_i(k+1)) + \hat{i}_{\mathrm{new}}(k+1)) + \hat{\omega}_r(k+1). \qquad (26)$$

After discretizing (10), the ESO can be obtained as

$$\begin{cases} e(k) = \hat{\omega}_r(k) - \omega_r(k) \\ \hat{\omega}_r(k+1) = T'_s(\hat{i}_{\mathrm{new}}(k) - \beta_1 e(k)) + \hat{\omega}_{\mathrm{r}}(k) \\ \hat{i}_{\mathrm{new}}(k+1) = T_s(\hat{f}_i(k) + \alpha_i v_q(k-1) - \beta_2 e(k)) + \hat{i}_{\mathrm{new}}(k) \\ \hat{f}_i(k+1) = -T_s\beta_3 e(k) + \hat{f}_i(k) \end{cases}. \qquad (27)$$

Obviously, the estimated values in (26) can be obtained by employing the high-order observer (27). One-step delay compensation is achieved by using the observer in discrete form.

By utilizing forward Euler discretization, the discrete equation for the d-axis current observer (17) is given by

$$\begin{cases} e_d(k) = \hat{i}_d(k) - i_d(k) \\ \hat{i}_d(k+1) = T_s(\hat{f}_d(k) + \alpha_d v_d(k) - \beta_4 e_d(k)) + \hat{i}_d(k) \\ \hat{f}_d(k+1) = -T_s\beta_5 e_d(k) + \hat{f}_d(k) \end{cases}. \qquad (28)$$

Similarly, a time delay of one sampling period is considered. The predictive equation for the d-axis current is as follows:

$$i_d(k+2) = T_s\alpha_d v_d(k) + T_s\hat{f}_d(k+1) + \hat{i}_d(k+1). \qquad (29)$$

Therefore, according to the response characteristics of mechanical and electrical quantities, after adopting the same update rates for speed and current, the expression of the motor's voltage

law can be defined as

$$\begin{cases} v_d = \frac{0-\hat{i}_d(k+1)}{T_s\alpha_d} - \frac{\hat{f}_d(k+1)}{\alpha_d} \\ v_q = \frac{\omega_r^{\text{ref}}-\hat{\omega}_r(k+1)}{10T_s^2\alpha_i} - \frac{\hat{i}_{\text{new}}(k+1)}{T_s\alpha_i} - \frac{\hat{f}_i(k+1)}{\alpha_i} \end{cases}. \tag{30}$$

As can be seen from (30), the predictive controller of the dq-axis voltage is close to a proportional controller [30], which further demonstrates the significance of its disturbance term for system control.

In practical systems, it is crucial to prioritize current constraints to prevent overloading of the motor system. Due to the absence of a q-axis current variable in the control system, a direct constraint is not feasible. Consequently, an estimation method is employed to estimate the q-axis current, and the q-axis voltage is limited to prevent overloading. Given the transient nature of current, mechanical disturbances are often considered negligible; therefore,

$$\dot{f}_\omega \approx 0. \tag{31}$$

Then, the relationship between the reconstructed current and the q-axis current can be restated as follows:

$$\alpha_\omega \dot{i}_q = \dot{i}_{\text{new}} = \alpha_i v_q + f_i. \tag{32}$$

Assuming the maximum allowable current for the motor is denoted as $i_{\max,}$ upon further discretization (32)

$$\alpha_\omega \frac{-i_{\max} - i_q(k)}{T_s} \le \alpha_i v_q + f_i \le \alpha_\omega \frac{i_{\max} - i_q(k)}{T_s}. \tag{33}$$

Then, the limit for the q-axis voltage is obtained by

$$\frac{(-i_{\max}-i_q(k))}{\alpha_q T_s} - \frac{\hat{f}_i(k)}{\alpha_i} \le v_q(k) \le \frac{(i_{\max}-i_q(k))}{\alpha_q T_s} - \frac{\hat{f}_i(k)}{\alpha_i}. \tag{34}$$

In summary, the implementation structure of RMPDSC is constructed based on the reconstructed model, and TESO is shown in Fig. 4. This control structure realizes the decoupling of speed and d-axis current through an observer, thus enabling parallel control. The control process starts with obtaining the measured values of basic variables from physical sensors. These measured values are then input into the observer to predict the aggregated disturbances of the model. Combined with the feedback variables and the predictive model, these disturbances generate the control voltage for the next control cycle. After amplitude limiting calculations (including current limiting and voltage limiting), the voltage undergoes pulsewidth modulation to form a control vector, which drives the motor to operate. The above-mentioned process is mainly divided into two interrupts during the operation of the processor: the serial communication interrupt, the current loop interrupt, which includes the speed closed-loop control program and the speed open-loop program.

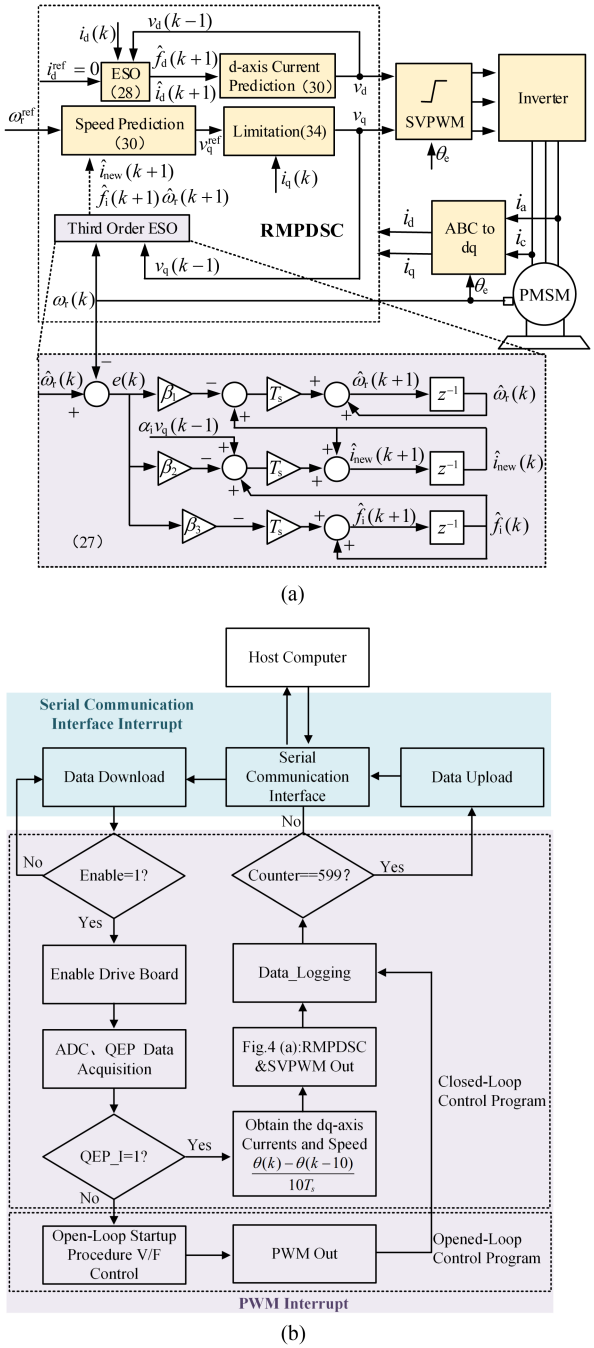

Fig. 4. Robust model predictive direct speed control based on TESO. (a) Control method structure. (b) Control program structure.

IV. Experimental Result

An experimental platform based on the TMSF28379D chip is constructed to verify the method proposed in this article, as shown in Fig. 5. The experimental platform utilizes an SPMSM with identical parameters to construct a dual-motor test platform (see Table I for platform parameters). During the experiment, real-time uploading of internal controller data to the host computer is achieved through serial communication. In the experiment, the dead-time of the inverter is 75 ns. In addition, the current sampling time is set to 100 μs. The speed update mechanism is shown in (35), so the speed sampling time is the same as the current sampling time.

The calculation formula for speed is as follows:

$$\omega_r(k) = \frac{\theta_r(k) - \theta_r(k-n)}{nT_s}. \tag{35}$$

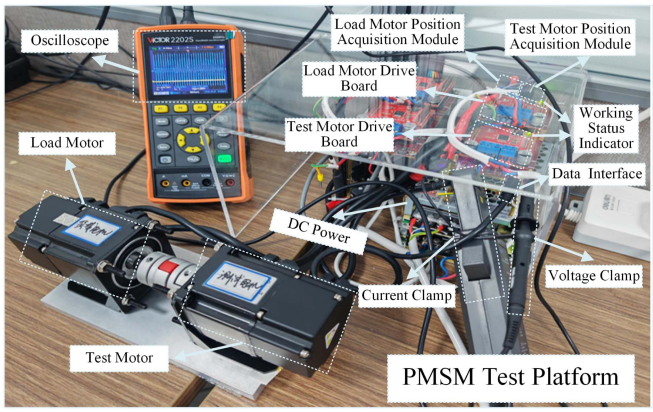

Fig. 5. Experiment Platform.

TABLE I
EXPERIMENTAL PLATFORM PARAMETERS

Symbol	Parameters	Value
R_s	Phase resistance	0.22 Ω
L_s	Phase inductance	1 mH
ψ	Flux linkage	0.1 Wb
P	Motor pole pairs	4
J	Moment of inertia	0.000023 kg·m^2
i_N	Rated current	5 A
$i_{\max}$	Maximum allowable current	10A
ω_N	Rated speed	2000 r/min
v_{dc}	Rated voltage	24 V

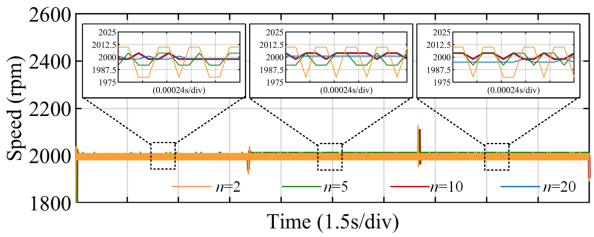

Fig. 6. Speed ripple under different speed sampling times.

The different calculation window times nT_s ($n = 2, 5, 10, 20$) of speed in the experiment were verified in Fig. 6. The results indicate that when the calculation window time is too low, the steady-state performance of the system will be affected, and the speed fluctuates significantly. However, issues affecting the system's dynamic performance will occur when the sampling multiple is too high. Therefore, the value of n is chosen to be 10.

The experimental verification mainly analyses the algorithm's performance from steady-state, dynamic, and anti-interference performance tests. To emphasize the distinctive features of the proposed method, it is compared and verified with two existing control methods: one is the predictive speed control method constructed based on cascaded disturbance compensation structure (PSC-CDCS [25], [26], [27]); the other is the model-free predictive current control method built on a PI controller and

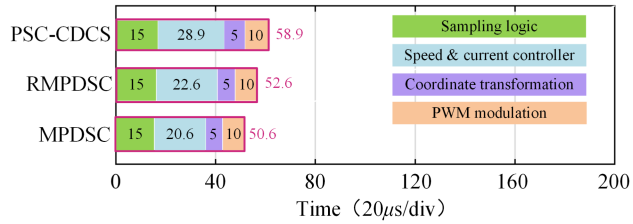

Fig. 7. Comparison of computational complexity of different control methods.

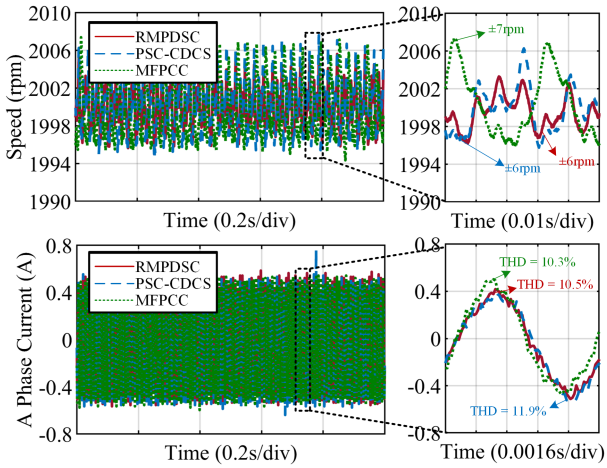

Fig. 8. Experimental results of speed and phase current under no-load conditions.

a single second-order ESO (such as MFPCC [3]). The method proposed in this article uses only one ESO to achieve the control of speed and q-axis current, and optimizes both the calculation structure and disturbance estimation. Therefore, compared with the multiobserver structure, this method has significantly improved in terms of computational complexity, and the comparison results are shown in Fig. 7 (among them, MPDSC is the model predictive direct speed control method without using an observer). Besides computational performance, the performance of these three methods in speed fluctuation suppression, speed overshooting, and external interference rejection will be tested next. Regarding parameter configuration, situations with similar steady-state performance are selected to facilitate comparison. The bandwidth of the TESO adopted in this article is set to 100 Hz. Among them, for PSC-CDCS, the bandwidth of the ESO in the speed loop is 50 Hz, and that in the current loop is 200 Hz; for MFPCC, the damping coefficient of the speed loop is set to 5 (a value greater than 1 indicates stability, and the larger this value is, the lower the control bandwidth of the speed loop is). The bandwidth of the current ESO is 200 Hz.

A. Steady-State Performance Test

Then, the steady-state performance of the three methods under no-load conditions was compared, and the experimental results are shown in Fig. 8. In the motor control experiment under no-load conditions, the RMPDSC proposed in this article demonstrates unique advantages. From the perspective of speed

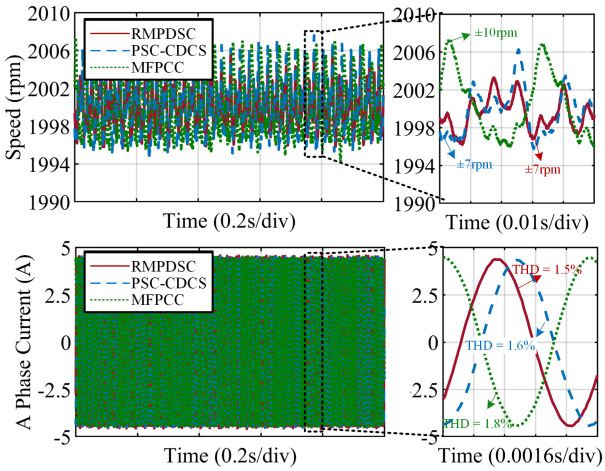

Fig. 9. Experimental results of speed and phase current under rated conditions.

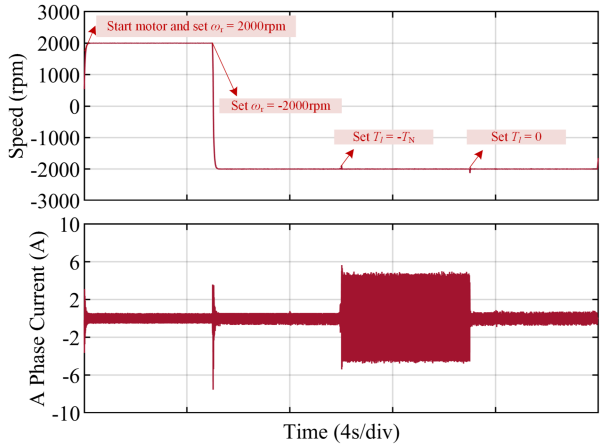

Fig. 10. Experimental results of speed forward and reverse rotation ability.

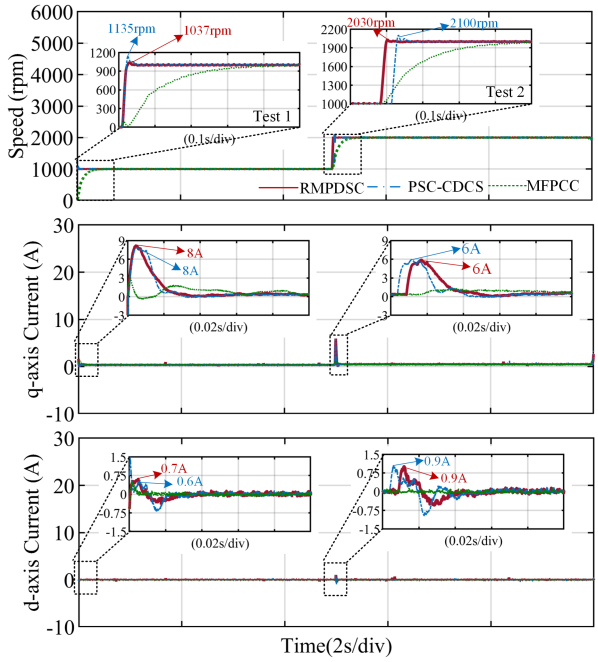

Fig. 11. Results of speed step experiment.

stability, the speed fluctuation range of RMPDSC is ±6 r/min, the same as that of PSC-CDCS and better than the ±7 r/min of MFPCC, indicating that RMPDSC can maintain the motor's speed stability more effectively. Regarding phase-current characteristics, the total harmonic distortion (THD) of RMPDSC is 10.5% . Although this value is slightly higher than the 10.3% of MFPCC, it is significantly lower than the 11.9% of PSC-CDCS. Therefore, compared with PSC-CDCS, RMPDSC can control current harmonics more effectively while ensuring speed stability. This steady-state performance test verifies that RMPDSC performs better in balancing speed and current quality. Considering both speed and current performance, it highlights its comprehensive advantage in motor control under no-load conditions.

Fig. 9 shows the experimental results of the steady-state performance tests on the motor control speed and phase current under rated conditions. Regarding speed steady-state performance, RMPDSC and PSC-CDCS speed fluctuations are ±7 r/min, significantly better than the ±10 r/min of MFPCC, demonstrating good speed control capabilities. Regarding phase current quality, the THD of RMPDSC is 1.5% , lower than the 1.6% of PSC-CDCS and 1.8% of MFPCC, indicating that it has a better effect on suppressing speed harmonics and higher current quality. Compared with PSC-CDCS, RMPDSC achieves a lower current THD while maintaining similar speed stability, showing more apparent advantages in overall performance.

B. Dynamic Performance Test

Considering that servo motors need a certain forward and reverse rotation ability, the proposed method's forward and reverse rotation ability was tested in Fig. 10. Experiments show that the proposed method has normal forward and reverse rotation and loading capabilities.

Figs. 11 and 12 test the dynamic performance of the system's speed. Test 1 is a step test from 0 to 1000 speed, test 2 is a step test from 1000 to 2000, test 3 is a sudden application of rated load test, and test 4 is a sudden reduction of load test. The dynamic performance of the reconstructed speed prediction structure is analyzed through these four tests. The performance of the speed is given in Table II. In test 1, the speed overshoot of RMPDSC is 3.7% , while that of PSC-CDCS reaches 13.5% . The overshoot of RMPDSC is reduced by approximately 72.6% compared with PSC-CDCS. In test 2, the overshoot of RMPDSC is 1.5% , and PSC-CDCS's is 5% , with a 60% reduction in overshoot. Regarding adjustment time, RMPDSC and PSC-CDCS are much faster than MPFCC, which indicates that RMPDSC has a stronger speed control performance and can track the target speed more quickly and stably. In test 3, the maximum speed drop of RMPDSC is 40 r/min, that of PSC-CDCS is 100 r/min, and that of MFPCC is 125 r/min. In test 4, the maximum speed fluctuation of RMPDSC is 25 r/min, that of PSC-CDCS is 90 r/min, and that of MFPCC is 130 r/min. It can be seen that the speed fluctuation range of RMPDSC is significantly smaller than that of the other two methods, closer to the target value,

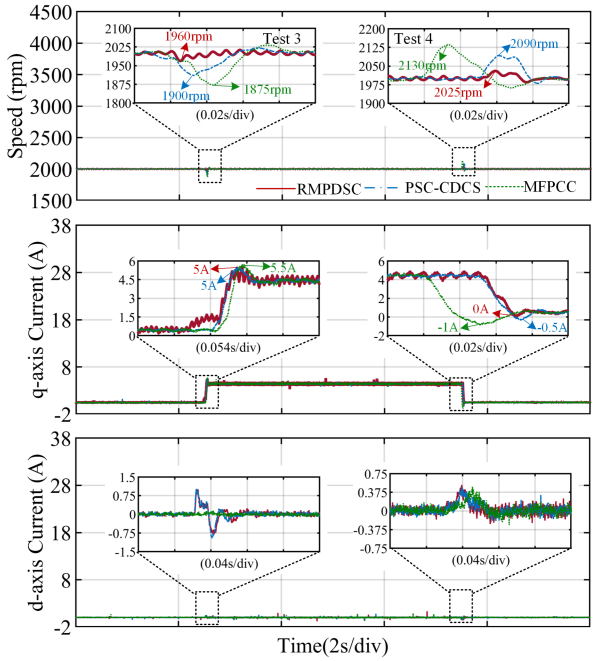

Fig. 12. Results of the torque step experiment.

TABLE II
EXPERIMENTAL RESULTS OF DYNAMIC PERFORMANCE

Test number	Method	RMPDSC	PSC-CDCS [25]–[27]	MFPCC [3]
1	Speed overshoot	3.7%	13.5%	0
	Adjustment time	0.1 s<	0.1 s<	>0.3 s
2	Speed overshoot	1.5%	5%	0
	Adjustment time	0.1 s<	0.1 s<	>0.3 s
3	Speed drop	40 r/min	100 r/min	125 r/min
	Adjustment time	0.02 s	0.04 s	0.07 s
4	Speed increase	25 r/min	90 r/min	130 r/min
	Adjustment time	0.02 s	0.03 s	0.06 s

and has a stronger anti-interference ability. Moreover, regarding adjustment time, RMPDSC has an obvious advantage and can effectively achieve high-precision speed control. Therefore, in terms of dynamic performance, RMPDSC has significant advantages.

Fig. 13 shows the experimental results of load-starting and load-braking under different current limiting conditions. A load is first applied to the power motor in the experimental process. It can be observed that the power motor generates an electromagnetic torque to resist the load torque and remain stationary, thus maintaining the speed at zero. Subsequently, the reference speed is set to 2000 r/min to start the power motor. The motor starts quickly with a load, and during this process, the phase current can be maintained near the set current limiting values of 5 and

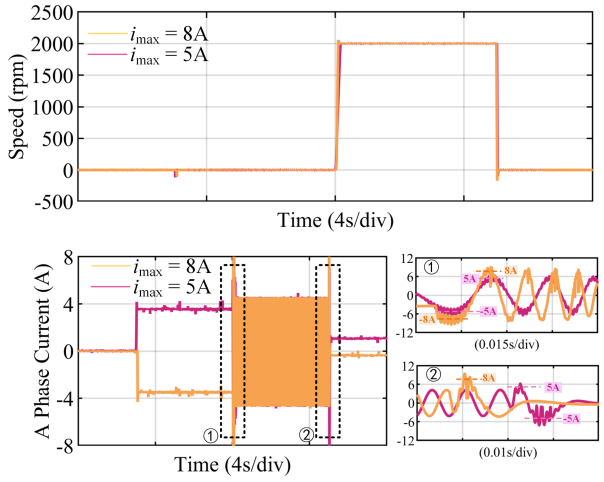

Fig. 13. Experimental results of current limiting during load-starting and load-braking processes.

8 A. Then, the reference speed is set to 0 for load-braking. It can be seen that the motor speed quickly returns to zero, but a torque is still generated to resist the load torque. During this process, the current is also maintained near the limiting value, with only a short-term ripple, which is acceptable for the motor system. The above experiments indicate that the method proposed in this article can effectively limit the current and is applicable to the working scenarios of load-starting.

C. Parameter Robustness Test of the Input Gain of ESO

When implementing the three methods of RMPDSC, PSC-CDCS, and MFPCC, it is still necessary to rely on motor parameters to consider the impact of the observer's input gain on speed control. In the RMPDSC proposed in this article, α_i is the input gain related to flux-linkage, inductance, and moment of inertia. Therefore, evaluating the experimental effects when one or more of these parameters change simultaneously is necessary to examine the system's robustness. In contrast, for the PSC-CDCS with a cascaded disturbance observer structure, it is necessary to consider both α_ω related to the moment of inertia J in the outer speed loop and the gain α_{q} related to the inductance in the inner current loop. MFPCC also needs to consider the gain α_q related to the inductance. Therefore, this article takes the actual motor parameters as the reference input gain, sets the input gains of the three methods to be 4 times and 0.25 times the reference value, respectively, and then conducts comparative experimental tests. Fig. 14 shows the experimental results of the three methods with an input gain of 0.25 times the reference value, specifically including four experimental scenarios (0.25 α_i for RMPDSC, 0.25 α_ω for PSC-CDCS, 0.25 α_q for PSC-CDCS, 0.25 α_q for MFPCC). From the perspective of speed stability under rated conditions, the THD of the speed fluctuation of RMPDSC is 0.20% , that of PSC-CDCS is 0.19% , that of PSC-CDCS2 is 0.24% , and that of MFPCC is 0.35% . The speed THDs of RMPDSC and PSC-CDCS (with the outer speed loop input gain reduced to 0.25

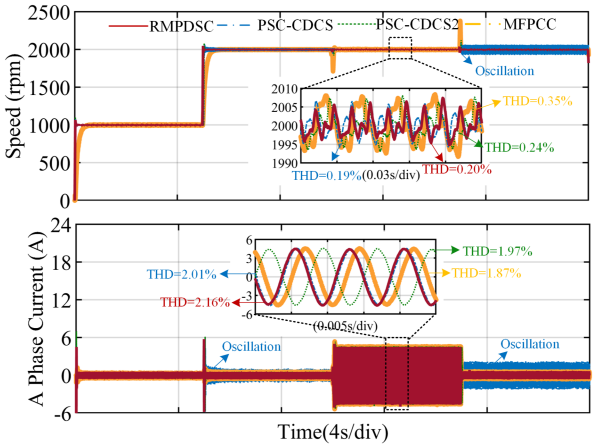

Fig. 14. Comparison of experimental results when the controller gain is reduced to 0.25 times, where the experimental result of MF HPPSC is when the outer loop gain α_ω changes, and the experimental result of MF HPPSC2 is when the inner loop gain α_q changes.

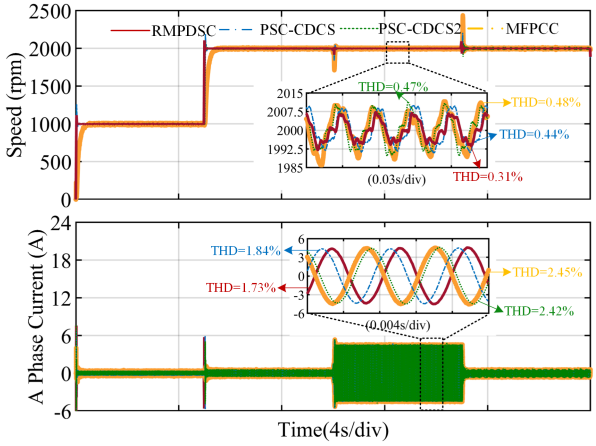

Fig. 15. Comparison of experimental results when the controller gain is reduced to four times, where the experimental result of PSC-CDCS is when the outer loop gain α_ω changes, and the experimental result of PSC-CDCS2 is when the inner loop gain α_q changes.

times) are relatively low. However, under no-load conditions, system oscillations occurred in PSC-CDCS. This experiment indicates that RMPDSC can still maintain better speed stability when the control gain is reduced, and changes in the moment of inertia significantly impact the stability of PSC-CDCS. The phase current's harmonic content needs to be analyzed to evaluate the motor's overall steady-state performance. In terms of the phase current, the THD of the phase current of MFPCC under rated conditions is the lowest, at 1.87% , and the THD of the phase current of RMPDSC is 2.16% , slightly higher than that of MFPCC, with a difference of 13% . The speed control target is crucial for system operation. The speed fluctuation of RMPDSC is 45% lower than that of MPPCC. In conclusion, RMPDSC performs better under the adverse condition of reduced control gain.

As shown in Fig. 15, an experimental comparison was carried out after increasing the motor control gains (4 α_i for RMPDSC, 4 α_ω for PSC-CDCS, 4 α_q for PSC-CDCS, and 4 α_q for MFPCC) of the three methods by a factor of four times. In terms of the THD of the speed, that of RMPDSC is 0.31% , significantly lower than 0.44% of MFHPPSC, 0.47% of MFHPPSC2, and 0.48% of MFPCC, indicating that RMPDSC has the best speed stability. Regarding the THD of the phase current, that of RMPDSC is 1.73% , superior to 2.42% of MFHPPSC2, 2.45% of MFPCC, and 1.84% of MFHPPSC. Under the harsh condition of a significant quadrupling of the control gain, RMPDSC ensures excellent performance and stability of the system with the lowest speed THD. Meanwhile, its phase current THD is also relatively low, demonstrating its good ability to control the comprehensive performance of speed and current when the gain changes. In addition, this article summarizes the gain caused by parameters into one parameter, which can offset the impact on the system when the inductance and flux linkage decrease simultaneously.

In the actual system, the motor's permanent-magnet flux linkage and inductance are prone to change. When the motor load is large, the current increases, and the inductance is likely to be saturated [32], decreasing the inductance value. Long-term operation will also cause the motor temperature to rise, thus reducing the flux linkage [33]. Therefore, the changes in the flux linkage and inductance are consistent. Based on this rule, the method proposed in this article equivalently regards the inductance and flux linkage as the denominator and numerator parameters, respectively. In this way, the consistency of the two changes is offset. Therefore, when the parameters change in Fig. 16, this method exhibits more stable control performance. However, when the speed loop and current loop are designed separately, due to the gain changes in both links, the system performance deteriorates further, generating significant steady-state harmonics.

In Section III-B, the influence of α_i on RMPDSC speed control was analyzed theoretically. The theory indicates that the system does not achieve the optimal speed dynamic performance when the value of α_i is precisely equal to the motor parameters, and this conclusion was verified in Fig. 17. During the speed transient process, a higher control gain increases the amplitude of speed fluctuations. For example, when α_i becomes four times (4 α_i), the speed drops to approximately 1919 r/min when torque is suddenly applied and increases to 2100 r/min when torque is suddenly removed. Moreover, the slow recovery speed reflects the system's poor load disturbance resistance. A lower control gain can reduce the speed fluctuations during the dynamic process. For instance, when the gain is 0.25 times (0.25 α_i), the speed decreases by 35 r/min when torque is suddenly applied and only increases by 45 r/min when torque is suddenly removed, and the recovery time is significantly shortened. Regarding the steady-state performance of the phase current, the closer the gain is to the reference value α_i, the lower the current harmonics. The gap in harmonic content is quite apparent under no-load conditions, but this gap narrows under rated conditions. Therefore, appropriately reducing the value of α_i helps improve the speed's dynamic performance.

Based on the abovementioned experiments, the RMPDSC proposed in this article simplifies the parameter-tuning process by reconstructing the model and reducing the control parameters to the control bandwidth of a disturbance observer. The speed

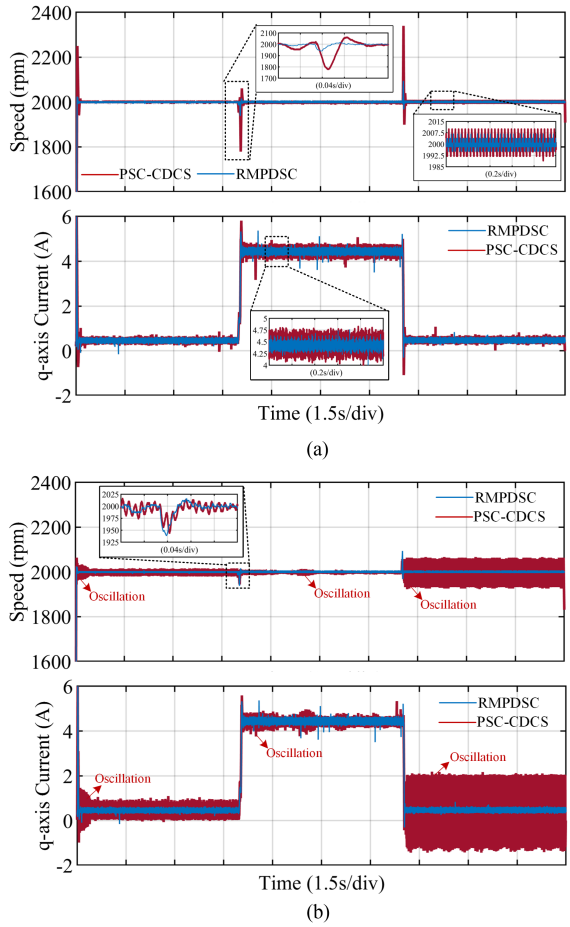

Fig. 16. Experimental results when inductance and magnetic flux linkage change simultaneously are as follows: (a) Both increase by two times. (b) Both decrease to 0.5 times.

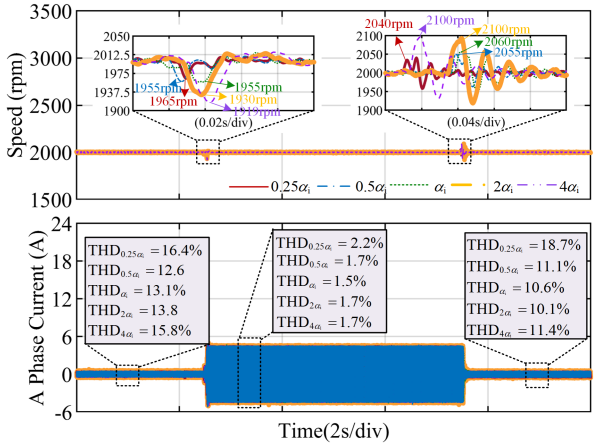

Fig. 17. Experimental results of RMPDSC under different input gains.

performance test results show that its dynamic and steady-state performances are superior to those of the PSC-CDCS and MFPCC methods with more parameters. Moreover, in dealing with input gain changes, this method can counteract the effects of multiparameter changes and has an absolute advantage in robustness.

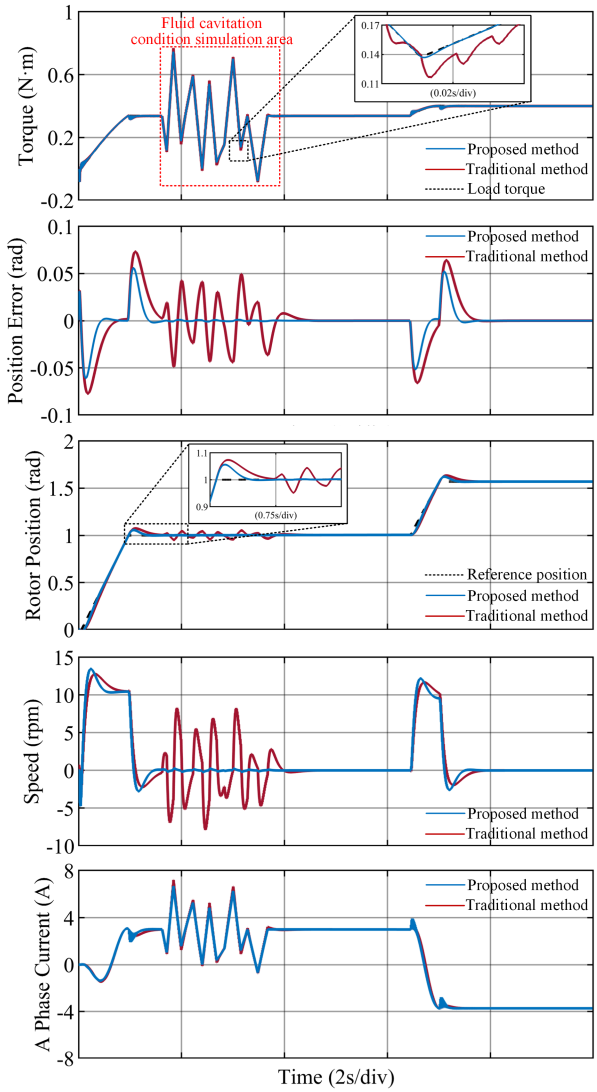

Fig. 18. Simulation results of RMPDSC applied to the servo system.

D. Analysis of Servo System Application Simulation

To further verify the application effectiveness of the proposed method in the servo control system, a simulation model of the servo-motor control system for the reversing device in the water-jet propulsion system is built. The load torque of the servo motor of the reversing device is related to the sine value of the rotation angle, and a load-torque model is constructed based on this. Moreover, random oscillations are applied under the stable state to simulate the torque fluctuations caused by fluid cavitation and test the proposed method's control effect on the rotor position and speed when oscillating torque disturbances occur. The simulation results are shown in Fig. 18. In this figure, the proposed method is compared with the vector control scheme adopted in the actual system. It can be clearly seen that the proposed method has a higher following accuracy of the load torque. When the cavitation phenomenon occurs and irregular torque oscillations are generated, the proposed method shows stronger speed control and position control robustness,

with a smaller following-angle error and a faster convergence speed. These simulation results verify that the proposed method has excellent dynamic performance and robustness in the servo device of the water-jet propulsion system.

V. Conclusion

This article proposes an RMPDSC method based on a TESO to solve the disturbance suppression problem in the direct speed control of PMSM, improve the dynamic performance of speed, and simplify the design of control parameters. First, the mathematical model of the PMSM is reconstructed, and the speed disturbance is equivalently transformed into part of the current lumped disturbance, thus enhancing the system's antidisturbance ability and dynamic performance. Subsequently, for the reconstructed second-order speed prediction equation, a corresponding TESO is designed to simplify the control structure of model-free direct speed control. The antidisturbance performance of the high-order ESO and its impact on system stability are presented through root locus and frequency-domain analysis. The focus is on analyzing the impact of the observer input gain on the system's dynamic performance, and it is pointed out that it is more appropriate for this value to be slightly less than the reference value constructed based on the motor parameters. Finally, experimental verification shows that compared with the model-free predictive direct speed control method using two observers to observe the speed and current disturbances respectively, and the model-free predictive current control method, the proposed RMPDSC method performs better in terms of stability, dynamic performance, and antidisturbance performance.

The direct speed control method discussed in this article is implemented using the forward Euler discretization method and physical rotor position sensors. Besides the forward Euler discretization method, other discretization methods, such as the trapezoidal method, may enhance the system's dynamic performance, and sensorless control methods can be used to improve the robustness of the speed. Therefore, applying the trapezoidal method and sensorless control methods to the speed prediction equation is an essential and promising scheme worthy of in-depth study, which can be regarded as one of the critical future research directions.

References

[1] P. G. Carlet, A. Favato, S. Bolognani, and F. Dörfler, "Data-driven continuous-set predictive current control for synchronous motor drives," *IEEE Trans. Power Electron.*, vol. 37, no. 6, pp. 6637–6646, Jun. 2022.

[2] J. Rodriguez, R. M. Kennel, J. R. Espinoza, M. Trincado, C. A. Silva, and C. A. Rojas, "High-performance control strategies for electrical drives: An experimental assessment," *IEEE Trans. Ind. Electron.*, vol. 59, no. 2, pp. 812–820, Feb. 2012.

[3] X. Yuan, S. Xie, J. Chen, S. Zhang, C. Zhang, and C. H. T. Lee, "An enhanced deadbeat predictive current control of SPMSM with linear disturbance observer," *IEEE J. Emerg. Sel. Topics Power Electron.*, vol. 10, no. 5, pp. 6304–6316, Oct. 2022.

[4] E. J. Fuentes, C. A. Silva, and J. I. Yuz, "Predictive speed control of a two-mass system driven by a permanent magnet synchronous motor," *IEEE Trans. Ind. Electron.*, vol. 59, no. 7, pp. 2840–2848, Jul. 2012.

[5] M. Abu-Ali, F. Berkel, M. Manderla, S. Reimann, R. Kennel, and M. Abdelrahem, "Deep learning-based long-horizon MPC: Robust, high performing, and computationally efficient control for PMSM drives," *IEEE Trans. Power Electron.*, vol. 37, no. 10, pp. 12486–12501, Oct. 2022.

[6] Y. Zhang, H. Jiang, and H. Yang, "Model predictive control of PMSM drives based on general discrete space vector modulation," *IEEE Trans. Energy Convers.*, vol. 36, no. 2, pp. 1300–1307, Jun. 2021.

[7] Z. Wang et al., "Deadbeat predictive current control of permanent magnet synchronous motor based on variable step-size adaline neural network parameter identification," *IET Electric Power Appl.*, vol. 14, no. 11, pp. 2007–2015, Nov. 2020.

[8] Z. Zhang, H. Guo, and Y. Liu, "DC-link voltage constraint strategy for DC power supply film-capacitor drive system based on improved model predictive control," *IEEE Trans. Ind. Electron.*, vol. 69, no. 10, pp. 9849–9859, Oct. 2022.

[9] F. Wang, S. Li, X. Mei, W. Xie, J. Rodriguez, and R. M. Kennel, "Model-based predictive direct control strategies for electrical drives: An experimental evaluation of PTC and PCC methods," *IEEE Trans. Ind. Inform.*, vol. 11, no. 3, pp. 671–681, Jun. 2015.

[10] S. Mariethoz, A. Domahidi, and M. Morari, "High-bandwidth explicit model predictive control of electrical drives," *IEEE Trans. Ind. Appl.*, vol. 48, no. 6, pp. 1980–1992, Nov./Dec. 2012.

[11] J. Mao et al., "Non-cascaded model-free predictive speed control of SMPMSM drive system," *IEEE Trans. Energy Convers.*, vol. 37, no. 1, pp. 153–162, Mar. 2022.

[12] M. Preindl and S. Bolognani, "Model predictive direct speed control with finite control set of PMSM drive systems," *IEEE Trans. Power Electron.*, vol. 28, no. 2, pp. 1007–1015, Feb. 2013.

[13] M. Liu, K. W. Chan, J. Hu, W. Xu, and J. Rodriguez, "Model predictive direct speed control with torque oscillation reduction for PMSM drives," *IEEE Trans. Ind. Inform.*, vol. 15, no. 9, pp. 4944–4956, Sep. 2019.

[14] X. Zhang and Y. He, "Direct voltage-selection based model predictive direct speed control for PMSM drives without weighting factor," *IEEE Trans. Power Electron.*, vol. 34, no. 8, pp. 7838–7851, Aug. 2019.

[15] P. Phowanna, S. Boonto, and M. Konghirun, "Online parameter identification method for IPMSM drive with MTPA," in *Proc. 18th Int. Conf. Elect. Machines Syst.*, Oct. 2015, pp. 1775–1780.

[16] P. H. Mellor, F. B. Chaaban, and K. J. Binns, "Estimation of parameters and performance of rare-earth permanent-magnet motors avoiding measurement of load angle," *IEE Proc. B Elect. Power Appl.*, vol. 138, no. 6, 1991, Art. no. 322.

[17] Y. Zhou, S. Zhang, C. Zhang, X. Li, X. Li, and X. Yuan, "Current prediction error based parameter identification method for SPMSM with deadbeat predictive current control," *IEEE Trans. Energy Convers.*, vol. 36, no. 3, pp. 1700–1710, Sep. 2021.

[18] X. Yuan, S. Zhang, and C. Zhang, "Improved model predictive current control for SPMSM drives with parameter mismatch," *IEEE Trans. Ind. Electron.*, vol. 67, no. 2, pp. 852–862, Feb. 2020.

[19] H. Thabet, M. Ayadi, and F. Rotella, "Ultra-local model control based on an adaptive observer," in *Proc. IEEE Conf. Control Appl.*,, Oct. 2014, pp. 122–127.

[20] H. Liu and S. Li, "Speed control for PMSM servo system using predictive functional control and extended state observer," *IEEE Trans. Ind. Electron.*, vol. 59, no. 2, pp. 1171–1183, Feb. 2012.

[21] Y. Zhang, J. Jin, and L. Huang, "Model-free predictive current control of PMSM drives based on extended state observer using ultralocal model," *IEEE Trans. Ind. Electron.*, vol. 68, no. 2, pp. 993–1003, Feb. 2021.

[22] X. Yuan, Y. Zuo, Y. Fan, and C. H. T. Lee, "Model-free predictive current control of SPMSM drives using extended state observer," *IEEE Trans. Ind. Electron.*, vol. 69, no. 7, pp. 6540–6550, Jul. 2022.

[23] Z. Zhang, Y. Liu, X. Liang, H. Guo, and X. Zhuang, "Robust model predictive current control of PMSM based on nonlinear extended state observer," *IEEE J. Emerg. Sel. Topics Power Electron.*, vol. 11, no. 1, pp. 862–873, Feb. 2023.

[24] X. Wu, J. Kang, M. Yang, T. Wu, and S. Huang, "Model-free deadbeat predictive current control for SPMSM based on adaptive gain extended state observer," *IEEE Trans. Transp. Electrific.*, vol. 11, no. 1, pp. 536–543, Feb. 2025.

[25] Y. Chen, C. Liu, S. Liu, and Z. Song, "A new cascaded adaptive deadbeat control method for PMSM drive," *IEEE Trans. Ind. Electron.*, vol. 70, no. 4, pp. 3384–3393, Apr. 2023.

[26] S. Gao, Y. Wei, D. Zhang, H. Qi, Y. Wei, and Z. Yang, "Model-free hybrid parallel predictive speed control based on ultralocal model of PMSM for electric vehicles," *IEEE Trans. Ind. Electron.*, vol. 69, no. 10, pp. 9739–9748, Oct. 2022.

[27] G. Zhang et al., "Computational efficient DSVM-based model predictive direct speed control for SPMSM drives with mechanical disturbance suppression," *IEEE J. Emerg. Sel. Topics Power Electron.*, vol. 13, no. 2, pp. 1673–1686, Apr. 2025.
[28] X. Lin et al., "Observer-based fixed-time control for permanent-magnet synchronous motors with parameter uncertainties," *IEEE Trans. Power Electron.*, vol. 38, no. 4, pp. 4335–4344, Apr. 2023.
[29] J. Han, "From PID to active disturbance rejection control," *IEEE Trans. Ind. Electron.*, vol. 56, no. 3, pp. 900–906, Mar. 2009.
[30] L. Wang, *PID and Predictive Control of Electrical Drives and Power Converters Using MATLAB /Simulink*. Singapore: Wiley, 2015.
[31] X. Lin, J. Liu, Z. Liu, Y. Gao, L. Peretti, and L. Wu, "Model-free current predictive control for PMSMs with ultralocal model employing fixed-time observer and extremum-seeking method," *IEEE Trans. Power Electron.*, vol. 40, no. 8, pp. 10682–10693, Aug. 2025.
[32] F. Fernandez-Bernal, A. Garcia-Cerrada, and R. Faure, "Determination of parameters in interior permanent-magnet synchronous motors with iron losses without torque measurement," *IEEE Trans. Ind. Appl.*, vol. 37, no. 5, pp. 1265–1272, Sep./Oct. 2001.
[33] D. Q. Dang, M. Saad Rafaq, H. H. Choi, and J.-W. Jung, "Online parameter estimation technique for adaptive control applications of interior PM synchronous motor drives," *IEEE Trans. Ind. Electron.*, vol. 63, no. 3, pp. 1438–1449, Mar. 2016.

Zhenrui Zhang was born in 1994 in Qingdao, Shandong Province, China. He received the Bachelor of Engineering degree in marine engineering from Yantai University, Yantai, China, in 2017 and the Ph.D. degree from in marine engineering from Dalian Maritime University, Dalian, China, in 2023.

He is currently a Full-Time Researcher with the Marine Equipment and Technology Institute, Jiangsu University of Science and Technology. His research interests include permanent magnet synchronous motor drive control, model predictive control, thin film capacitor drive systems, and shipborne electric propulsion systems.

Xingyu Wang was born in 1989 in Jinzhou City, Liaoning Province, China. He received the B.S. degree in electrical engineering and automation and the M.S. degree in electrical engineering from Liaoning University of Engineering and Technology, Fuxin, China, in 2014 and 2017, respectively, and the Ph.D. degree in power electronics and electric drive from Northeastern University, Shenyang, China, in 2022.

He is with the Marine Equipment and Technology Institute, Jiangsu University of Science and Technology, China. His research interests include robotic manipulator motion control, server drive systems, intelligent manufacturing, sliding electrical contact, and basic theory of electrical equipment.

Jing Xu received the Ph.D. degree in mechanical engineering from the China University of Mining and Technology, Xuzhou, China, in 2018.

He is currently an Associate Professor of mechatronic engineering with the Marine Equipment and Technology Institute, Jiangsu University of Science and Technology, Zhenjiang, China. His research interests include signal processing, pattern recognition, and intelligent systems.

Qingya Zhang born in 1990 in Lianyungang, Jiangsu Province, China. He received the Bachelor's degree in engineering from Nanjing Institute of Technology, Nanjing, China, in 2014,and the master's degree in engineering from Jiangsu University of Science and Technology in 2017, and the Ph.D. degree in engineering from Huazhong University of Science and Technology, Huazhong, China, in 2022.

He is currently a Full-Time Researcher with the Marine Equipment and Technology Institute, Jiangsu University of Science and Technology, Zhenjiang, China. His research interests include intelligent servo drive systems and mechanical engineering.